Critical island size, scaling, and ordering in colloidal nanoparticle self-assembly

Chakra P. Joshi,[1] Yunsic Shim,[2] Terry P. Bigioni,[1] and Jacques G. Amar[2]
[1]*Department of Chemistry, University of Toledo, Toledo, Ohio 43606, USA*
[2]*Department of Physics & Astronomy, University of Toledo, Toledo, Ohio 43606, USA*
(Received 6 March 2014; published 29 September 2014)

In order to obtain a better understanding of short-range (SR) and long-range (LR) nanoparticle (NP) interactions during the self-assembly of dodecanethiol-coated Au NPs in toluene via drop drying, we have investigated the dependence of the island density, scaled island-size distribution (ISD), and scaled capture-zone distribution (CZD) on coverage, deposition flux, and NP size. Our results indicate that, while the critical island size is larger than 1 for all NP sizes studied, due to the increase in the strength of the SR attraction between NPs with increasing NP size, both the exponent describing the dependence of the island density on deposition flux and the critical island-size decrease with increasing NP size. We also find that, despite the existence of significant cluster diffusion and coalescence, the ISD is sharply peaked as in epitaxial growth. In particular, for large NP size, we find good agreement between the scaled ISD and epitaxial growth models as well as good agreement between the scaled CZD and scaled ISD. However, for smaller NPs the scaled ISD is less sharply peaked despite the fact that the critical island size is larger. This latter result suggests that in this case additional effects such as enhanced island coalescence or NP detachment from large islands may play an important role. Results for the ordering of NP islands are also presented which indicate the existence of LR repulsive interactions. One possible mechanism for such an interaction is the existence of a small dipole moment on each NP which arises as a result of an asymmetry, driven by surface tension, in the thiol distribution for NPs adsorbed at the toluene-air interface. Consistent with this mechanism, we find good agreement between experimental results for the nearest-neighbor island-distance distribution and simulations which include dipole repulsion.

DOI: 10.1103/PhysRevE.90.032406 PACS number(s): 68.43.Jk, 81.07.−b, 68.55.A−, 81.16.Dn

I. INTRODUCTION

Recently there has been a lot of interest in the formation of nanostructures via nanoparticle (NP) self-assembly using a variety of nonequilibrium processes ranging from evaporation to dewetting to flows [1–11]. In these studies, the self-assembly process has been found to involve several distinct types of interactions including ligand-ligand [1–3], van der Waals [12–15], magnetic [4], and Coulomb [11] interactions. As a result, a fundamental understanding of NP interactions, in particular at interfaces, is crucial in order to understand the self-assembly process.

One method of particular interest, which has been shown to lead to the formation of highly ordered nanocrystal monolayers [1–3], is the drop drying of ligand-coated NPs in solution. As shown in Fig. 1, in this method, a small drop of ligand-coated NPs in solution is placed on a Si chip and then allowed to evaporate in ambient conditions. As the droplet evaporates, NPs in solution are swept up by and adsorbed onto the interface. The adsorbed NPs then diffuse and aggregate to form NP islands on the droplet surface.

In drop-drying experiments on 6 nm core-diameter dodecanethiol-coated Au NPs in toluene [3] it was shown that the self-assembly process is controlled by the evaporation kinetics as well as by interactions between the NPs and the solvent-air interface. In particular, the deposition rate is determined by the evaporation rate of the droplet combined with the NP concentration. In addition, the nanoparticles act as surfactants and are bound to the surface of the toluene drop for a finite residence time which is determined by the strength of the interaction with the interface. The coverage of ligands on the nanoparticle determines the strength of binding to the toluene-air interface, while the ligand coverage is itself determined by the excess thiol concentration (free ligands) in solution.

For low NP and excess thiol concentrations, island formation is not observed [3] since the low binding energy leads to a desorption rate which is large compared to the deposition rate. For somewhat larger NP and excess thiol concentrations, island formation is observed although the diffusion length δ (corresponding to the typical distance a NP can diffuse before desorbing from the interface) is smaller than the typical distance between islands. In this case the coverage θ (corresponding to the fraction of a monolayer covered by islands) increases superlinearly with time [3] since the capture zone increases with increasing island size. However, for sufficiently high NP and excess thiol concentrations, it was found [3] that the diffusion length is larger than the typical distance between islands. As a result, in this regime all NPs reaching the interface are added to islands, and the coverage increases linearly with time.

While these results suggest that in this regime the nucleation and growth of NP islands may be similar to epitaxial growth, it should be noted that there are some major differences. In particular, island diffusion and coalescence are expected to play a much more important role in drop drying than in epitaxial growth. In addition, long-range (LR) interactions may affect NP island diffusion and ordering at high coverage. In this connection, we note that while the dependence of *average* quantities such as the diffusion length and average island-growth rate on excess thiol concentration was studied in Ref. [3], the scaling behavior of the island-size distribution and island density were not studied. An analysis of this scaling behavior provides an important opportunity to obtain a better understanding of the self-assembly process as well as of the

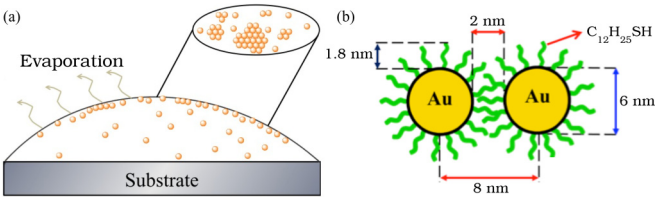

FIG. 1. (Color online) Schematic diagram of (a) growth of NP islands at the toluene-air interface (circles represent individual NPs) and (b) binding of dodecanethiol-ligated Au NPs of size 6 nm.

short-range (SR) and LR interactions between NPs adsorbed at the toluene-air interface.

Here we present results for the dependence of the island density on deposition flux and NP size for dodecanethiol-coated Au NPs in toluene which we have used to estimate the critical island size as well as the strength of the NP interactions at the interface. Our results indicate that, while the critical island size is larger than 1 for all NP sizes studied, due to the increase in the strength of the SR attractive interaction between NPs with increasing NP size, both the exponent χ describing the dependence of the island density on deposition flux and the critical island size decrease with increasing NP size. In addition, we present results for the scaled island-size distribution (ISD) and capture-zone distribution (CZD), and their dependence on NP size. Surprisingly, we find that, despite the existence of significant cluster diffusion and coalescence, which has been previously shown [16–19] to dramatically broaden the island-size distribution for the case of a critical island size of 1, in our experiments the scaled island-size distribution is sharply peaked as in epitaxial growth. In particular, for large NPs, we find good agreement between the scaled ISD and epitaxial growth models as well as good agreement between the scaled CZD and scaled ISD. However, for smaller NPs the scaled ISD is somewhat broader despite the fact that the critical island size is larger. This latter result suggests that additional effects such as enhanced island coalescence, NP detachment from large islands, or NP desorption in the early stages of growth may play an important role for smaller NPs.

Finally, we present experimental results for the ordering of NP islands which indicate the existence of a significant LR repulsive interaction. One possible mechanism for such an interaction is the existence of a small net dipole moment p on each NP which occurs as a result of an asymmetry in the distribution of thiols attached to adsorbed NPs. Consistent with this mechanism, we find good agreement between Monte Carlo simulations which take into account dipole repulsion and experimental results for the nearest-neighbor edge-distance distribution between islands. As expected for an interaction which depends on the NP surface area, we also find that the value of p increases with increasing NP size, while for fixed NP size, it decreases with increasing coverage. The corresponding enhancement of island coalescence due to the decrease of the dipole interaction with decreasing NP size also provides a possible explanation for the differences between the experimental ISD and CZD and the predictions of epitaxial growth models for smaller NP sizes.

This paper is organized as follows. In Sec. II we provide experimental details for submonolayer dodecanethiol (DDT)-ligated NP island growth. In Sec. III we first present our results for the dependence of the island density on coverage and for the dependence of the critical island size on NP size. We then present results for the dependence of the scaled island-size distribution and capture-zone distribution on NP size and compare with epitaxial growth theory. In Secs. III D and III E, we discuss the ordering of NP islands and present results for the nearest-neighbor edge-distance distributions obtained from experiment and simulations. Finally, we summarize our results in Sec. IV.

II. EXPERIMENTAL DETAILS

A. Materials

Sodium borohydride ($NaBH_4$) (Alfa Aesar, 98%), gold (III) chloride ($AuCl_3$) (Sigma Aldrich, 99%), dimethyldidodecylammonium bromide (DDAB) (Fisher, 98%), 1-dodecanethiol (Sigma Aldrich, 98%), ethanol (Fisher), and acetone (Fisher) were used without further purification. Toluene (Fisher) was dried using molecular sieves. Single-side polished silicon wafers were obtained from Nova Electronic Materials.

B. Synthesis of nanoparticles

Gold NPs were synthesized according to the Lin *et al.* [20] protocol. Briefly, 0.156 g of DDAB was added to 15 ml of dry toluene in a 500 ml round-bottomed flask and stirred. Next, 0.052 g of $AuCl_3$ was added into the same flask and sonicated until fully dissolved. While stirring at 800 rpm, 54 μl of aqueous $NaBH_4$ (9.7 M) solution was added drop by drop to the solution. In about 5 min, the yellowish-red $AuCl_3$ solution changed to yellow, then brown-yellow, and finally turned to a purple color after about 10 min, indicating formation of polydisperse gold nanoparticles [20]. Once formed, the nanoparticles were ligated by adding 1.2 ml of dodecanethiol (DDT) to the solution and were cleaned by precipitation with ethanol. The precipitate was dried under vacuum.

The broad size and shape distribution was improved by digestive ripening, which produced the spherical and monodisperse nanoparticles required for this study [20,21]. We note that in contrast to Ostwald ripening, in which large particles grow at the expense of smaller ones, the digestive ripening process [20] occurs through the transfer of material from large particles to small particles. For digestion, the raw Au NP product was redissolved in 16.2 ml of toluene with 7.4% DDT (v/v) and then heated at 110 °C for 3 hours, which redistributed mass and focused the NP sizes and shapes [1,20]. After digestion, the solution was kept at 60 °C overnight to allow larger particles to settle [1]. The top half of the solution, containing the most monodisperse NPs, was collected and used for the experiments.

The thiol concentration of the as-synthesized Au NPs was 7.4%. Repeated precipitation with ethanol and redispersion in toluene was used to clean the excess thiol from the solution. This was repeated until the NPs no longer stuck to the air-liquid interface [3]. The excess thiol concentration at this point was assumed to be zero and was then adjusted to suit the needs of the experiment (typically 1×10^{-3} by volume). Before each experiment, the NP solution was centrifuged at 14 000 rpm for

7 minutes to remove aggregates and other solids that might be present in the solution.

C. Video microscopy

A 50 μl drop of Au NPs was deposited on a 10 mm $\times$ 10 mm Si chip such that the drop was pinned by the edges of the substrate. This was done in an enclosed space to minimize the effect of the surrounding air currents. The drop was then allowed to evaporate under ambient conditions. An Olympus BX-61 microscope was used with an Olympus DP71 digital camera, capable of capturing 1.4 Mpix images at a rate of 15 fps. Images were extracted from these videos and analyzed using ImagePro Plus.

We note that due in part to hydrodynamic effects there are surface flows near the edge of the droplet which can lead to inhomogeneities. To minimize these effects, imaging of island formation was done in the center of the droplet. In addition, only regions with relatively uniform island densities and growth rates were studied since this indicated a uniform flux of nanoparticles onto the liquid-air interface. For the purposes of analyses, movies with similar island densities and fluxes were chosen to form a set of data since the experimental conditions were similar.

III. RESULTS

In order to study the dependence of the self-assembly process on NP size, we have carried out experiments for three different NP sizes with Au core diameters d equal to 4.9 ± 0.3 nm, 6.0 ± 0.4 nm, and 8.0 ± 0.4 nm. In most of these experiments the excess thiol concentration was 0.1% by volume fraction, while, unless otherwise noted, the NP concentrations were $3.2 \times 10^{11}/\mu$l, $1.7 \times 10^{11}/\mu$l, and $0.38 \times 10^{11}/\mu$l for 4.9 nm, 6.0 nm, and 8.0 nm NPs, respectively. Figures 2(a)–2(c) show optical microscopy images of NP islands formed at the toluene-air interface at three different coverages (where the fractional coverage $\theta = 0.1$, 0.28, and 0.44 monolayer or ML) for a NP Au core diameter $d = 6.0$ nm, while Figs. 2(d)–2(f) illustrate typical Voronoi cell structures around islands for three different NP sizes at fixed coverage ($\theta = 0.05$ ML). As can be seen, at low coverage the islands are generally compact and circular. On the other hand, at higher coverages the NP islands become somewhat elongated and irregular due to island diffusion, coalescence, and slow relaxation. Such a high island mobility is typically not present in the epitaxial growth of metal or semiconductor islands. This clearly indicates the distinctive difference between the current drop-drying technique and other conventional growth techniques, such as epitaxy, sputtering, and vapor deposition.

A. Dependence of island density on coverage and NP size

In order to compare with epitaxial growth we have studied the dependence of the island density on coverage and NP size in the submonolayer regime. As can be seen in Fig. 3(a), for all three NP sizes the coverage increases linearly with time, thus indicating a constant deposition rate or flux as well as the fact [3] that over this coverage range the monomer diffusion length is significantly larger than the typical distance between islands, and as a result, there is minimal monomer desorption.

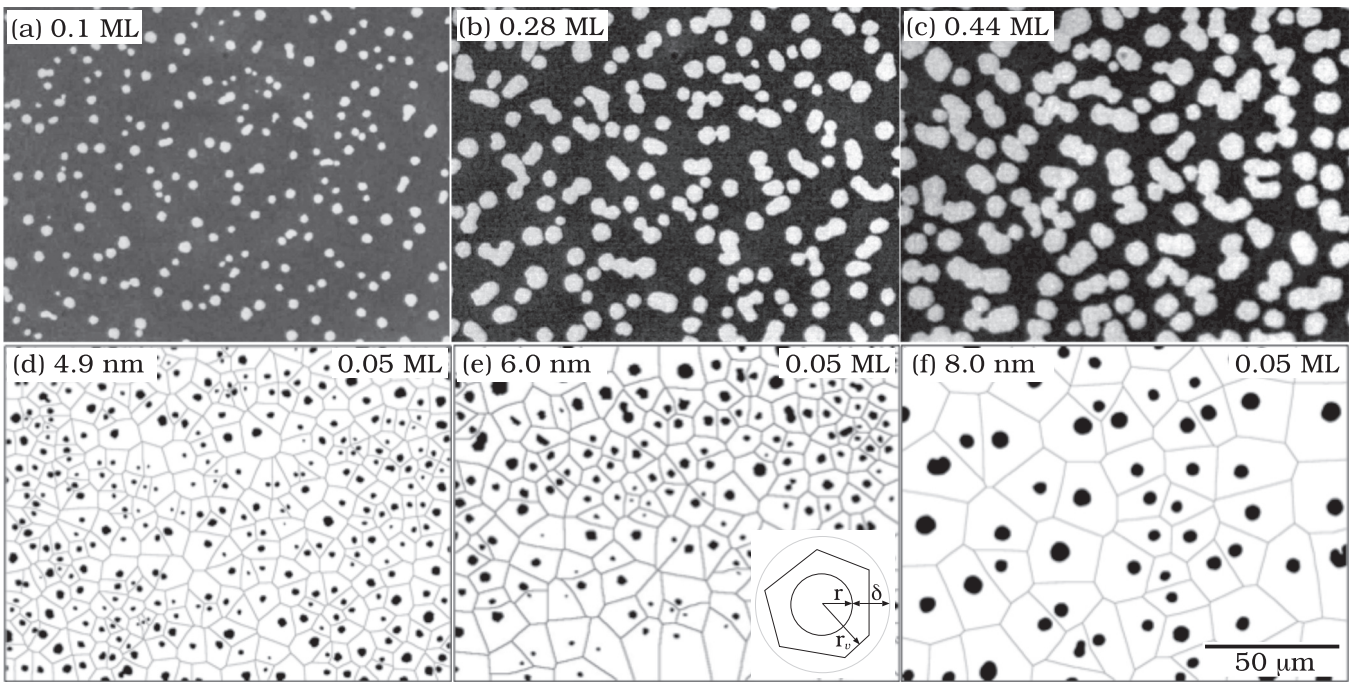

FIG. 2. (a)–(c) Optical microscope images of island growth of DDT-ligated 6 nm Au NPs at coverages of 0.1 ML, 0.28 ML, and 0.44 ML. (d)–(f) Voronoi cell structures around islands at $\theta = 0.05$ ML for three NP sizes: 4.9 nm, 6.0 nm, and 8.0 nm. Inset to panel (e) shows a schematic Voronoi cell of radius r_v for a circular island of radius r (monomer diffusion length δ) corresponding to the case studied here in which $r + \delta > r_v$.

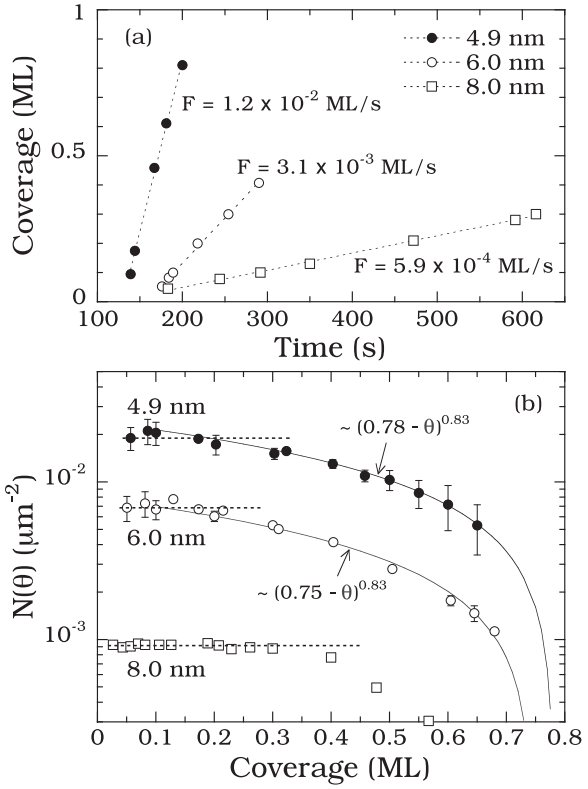

FIG. 3. (a) Dependence of coverage on time for three different NP sizes. For details on growth conditions see text. (b) Corresponding results for the island density $N(\theta)$ as a function of coverage. Solid lines are fits of the form $N(\theta) \sim (\theta_p - \theta)^{0.83}$.

By analogy with epitaxial growth, we may now define the monomer "hopping rate" $D_h = 4D/a^2$, where a is the "hopping distance" (assumed to be equal to the nearest-neighbor distance between NPs in a NP island) and D is the monomer diffusion coefficient, which may be approximated using the Stokes-Einstein relation,

$$D = \frac{k_B T}{6\pi\eta r_h}, \tag{1}$$

where η is the viscosity of toluene and r_h is the hydrodynamic radius of the NP. Since the DDT ligand length is approximately 1.8 nm (see Fig. 1), the hydrodynamic radius may also be estimated using the expression

$$r_h \simeq d/2 + 1.8 \text{ nm}. \tag{2}$$

We note that in recent molecular dynamics simulations [22] of the diffusion of a DDT-coated 6 nm NP adsorbed at the toluene-vapor interface, good agreement was found between simulation results for the monomer diffusion coefficient D and the corresponding predicted value ($D = 76\mu^2$/s) obtained using Eqs. (1) and (2).

Dividing D_h by the deposition flux F in ML/s, we may define the dimensionless quantity $R = D_h/F$ corresponding to the ratio of the monomer hopping rate to the deposition flux. Using Eqs. (1) and (2) with $\eta \simeq 0.59$ cP at $T =$ 293 K, along with the values of F shown in Fig. 3(a) and the nearest-neighbor distances $a = 6.9$ nm, 8.0 nm, and 9.6 nm for 4.9, 6.0 and 8.0 nm diameter NP islands respectively, leads to the values $R = 6.0 \times 10^8$ for 4.9 nm NPs, $R = 1.5 \times 10^9$ for 6.0 nm NPs, and $R = 4.6 \times 10^9$ for 8.0 nm NPs. These values are consistent with the range of typical values ($R = 10^5$–10^{11}) found in epitaxial growth.

Figure 3(b) shows the corresponding results for the dependence of the island density N on coverage θ in ML. As can be seen, the island density decreases with increasing NP size, which is consistent with the increase in the value of R with increasing NP size. In addition, for the largest (8 nm) NP size, the island density remains relatively constant up to a coverage $\theta = 0.3$. On the other hand, for the smaller NP sizes, there is significant coalescence above a coverage of 0.2 ML, which leads to a decrease in the island density with increasing coverage. We note that for both the 4.9 nm and 6.0 nm NPs [see Fig. 3(b)] the dependence of the island density on coverage can be approximately fit at high coverage using the "percolation-like" form $N(\theta) \sim (\theta_p - \theta)^{0.83}$ where the value of θ_p ($\theta_p \simeq 0.75$–0.78) is in good agreement with that obtained for disk percolation ($\theta_p^{\text{disk}} \sim 0.74$–$0.78$) [23].

B. Scaling exponent χ and critical island size

We now consider the dependence of the island density on deposition flux. One concept which has proved useful in the analysis of epitaxial submonolayer island nucleation and growth [24–31] is that of a critical island size i, corresponding to one less than the number of atoms or particles in the smallest stable island (see Fig. 4). In particular, in the case of monomer deposition and diffusion, but in the absence of desorption, cluster diffusion, or a barrier to the attachment of monomers to islands, standard nucleation theory (SNT) [24,31] predicts that the island density N in the precoalescence regime scales as

$$N \sim R^{-\chi} \exp\left[\frac{E_i}{(i+2)k_B T}\right], \tag{3}$$

where E_i is the binding energy of the critical island of size i, T is the substrate temperature and k_B is Boltzmann's constant. For the case of epitaxial growth with isotropic monomer diffusion but no cluster diffusion, SNT [24,31] also predicts $\chi(i) = i/(i+2)$. We note that at fixed temperature, Eq. (3) also implies that $N(F) \sim F^{\chi}$.

Figure 5 shows a log-log plot of our experimental results for the dependence of the island density N on deposition flux F at coverage $\theta = 0.05$ for all three NP sizes. In each case the NP concentration was varied in order to vary the

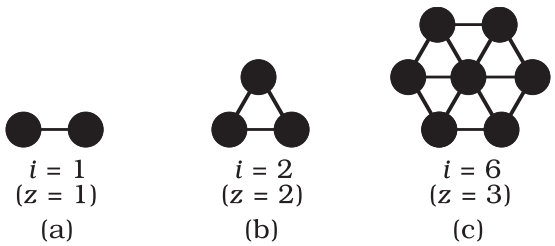

FIG. 4. Schematic showing critical island size i along with corresponding stable islands of size $i+1$, obtained assuming a bond-counting model with z nearest-neighbor bonds needed for stability.

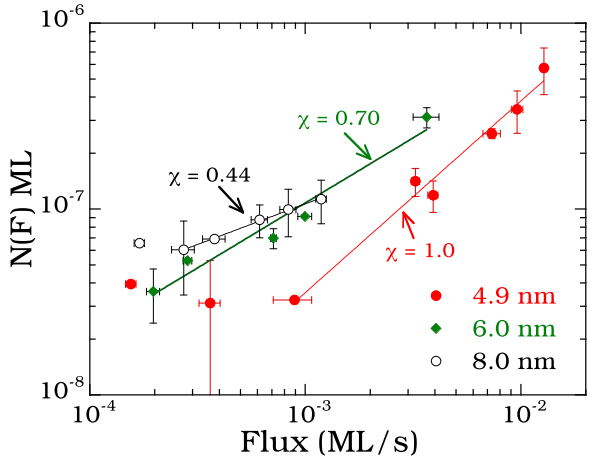

FIG. 5. (Color online) Island density N as a function of flux F at $\theta = 0.05$ ML for NP sizes of 4.9 nm, 6.0 nm, and 8.0 nm. Solid lines are power-law fits.

deposition flux [32]. For very small flux ($F < 2 \times 10^{-4}$ ML/s) the island density appears to decrease slightly with increasing deposition flux. However, for larger flux, it exhibits a power-law dependence on flux with an exponent χ which increases with decreasing NP size. In particular, for 8 nm NPs we find $\chi \simeq 0.44$ which is close to the value ($\chi = 1/2$) expected using SNT [24,31] for a critical island size equal to 2, corresponding to a stable trimer in which each NP has at least two nearest-neighbor bonds [see Fig. 4(b)]. In contrast, for the 6 nm NP we find $\chi \simeq 0.7$, which corresponds using SNT to a significantly larger effective critical island size ($i \simeq 4.7$). This value of χ is also close to the value ($\chi = 3/4$) expected for a critical island of size 6, which corresponds to one less than the number of NPs in a "magic" [33] island of size 7 [see Fig. 4(c)] in which each NP has at least three nearest-neighbor bonds. Finally, for the 4.9 nm NP we find $\chi \simeq 1.0$, which corresponds using SNT to a very large critical island size. Table I shows a summary of these results along with the corresponding values of the critical island size i.

We note that these results are consistent with estimates for the dimer binding energy which may be obtained using an effective interaction potential for NPs in toluene which was developed by Khan *et al.* [15], and which takes into account the solubility of dodecanethiol in toluene, the van der Waals attraction [12] between the Au cores, and the ligand-ligand interaction. In particular, applying this potential to the case of 8 nm NPs, a relatively large value of the dimer binding energy ($E_2/k_BT \simeq 8.5$ at room temperature) is obtained. This implies that compact islands of size 3 or larger, in which all NPs have at least two nearest-neighbor bonds (corresponding to an activation energy for detachment $E_a/k_BT \simeq 17$ at room temperature) should be relatively stable, thus indicating $i \simeq 2$ and $\chi \simeq 0.5$. In contrast, the smaller estimated dimer binding energy for 6 nm NPs ($E_2/k_BT \simeq 4.7$) is consistent with an effective minimum stable island of size 7 ($i \simeq 6$), which implies $\chi \simeq 0.75$ in reasonable agreement with experiment. Finally, for 4.9 nm NPs, the estimated dimer binding energy ($E_2/k_BT \simeq 3.0$) is sufficiently small that even islands of size 7 are not stable. As a result, the effective critical island size is significantly larger than 6, while the effective value of χ is close to 1. In this connection, the effects of island diffusion and coalescence on the exponent χ (assuming $D_A \sim A^{-\mu}$ where D_A is the diffusion constant for an island of area A and $0 < \mu < \infty$) have been studied both for the case of irreversible growth with $i = 1$ [16–18,34] as well as more recently for higher values of i [35,36]. In all cases it has been found that, assuming no barrier to island coalescence, the effective value of χ ranges between a value of $1/2$ for small μ and the standard prediction $i/(i+2)$ for large μ.

TABLE I. Critical island size i for three possible scenarios as a function of NP size. Here standard, attachment limited aggregation (ALA), and small cluster mobility (SCM) correspond to the expressions $\chi = i/(i+2)$, $2i/(i+3)$, and $i^*/(2i^*+1)$, respectively.

NP size	χ	Critical island size i		
		Standard	ALA	SCM (i^*)
4.9 nm	1.0 ± 0.2	∞	3.0	<0
6.0 nm	0.7 ± 0.2	4.7	1.6	<0
8.0 nm	0.44	1.6	0.85	3.7

For comparison, we consider several other nucleation models which lead to somewhat different expressions for χ as a function of critical island size i. For example, in the presence of a significant energy barrier for NPs to attach to island edges (corresponding to attachment limited aggregation or ALA) but in the absence of cluster diffusion a modified expression for the exponent $\chi = 2i/(i+3)$ has been predicted [37]. This implies $i = 1.6$ and 3.0 for 6.0 nm and 4.9 nm NPs respectively (see Table I). However, the ALA value for 4.9 nm NPs is not close to an expected critical island size, while both values are not consistent with our expectation of significant two-bond detachment for these NP sizes. In addition, the ALA value of $i \simeq 1$ for 8 nm NPs is not consistent with our expectation, based on estimates [36] of the prefactor and detachment barrier obtained using the Khan *et al.* potential [15], that dimers are unstable even for 8 nm NPs. We also note that recent work [38] on the ALA model indicates that in many cases this may lead to an extended nucleation regime in which the island density only saturates at large coverage. Similarly, for the small cluster mobility model [39,40] or SCM, in which all islands are stable ($i = 1$), but all islands of size $s \leqslant i^*$ are mobile with the same mobility, while larger islands are immobile, the exponent $\chi^{\rm SCM} = i^*/(2i^*+1)$. However, this implies a maximum value of χ ($\chi = 1/2$), which is significantly smaller than that obtained for 6 nm and 4.9 nm NPs.

Finally, in the case of monomer desorption but no cluster diffusion, such that the diffusion length for a monomer is shorter than the typical island separation, Jensen *et al.* have presented scaling arguments [41] (based on the assumption that the Walton relation [42] holds for $i > 1$ in the presence of desorption) that indicate that $\chi = 2i/3$. However, this implies a minimum value of $2/3$ for χ, along with a value of $4/3$ or higher for larger critical island size, which is inconsistent with our results for 4.9 nm and 8 nm NPs. Accordingly, we conclude that, while it does not directly take into account the effects of island diffusion and coalescence, standard nucleation theory appears to give reasonable results for the exponent χ.

C. Scaled island and Voronoi cell size distributions

1. Scaling and analytical expressions

We now consider the scaled island-size distribution (ISD) and Voronoi cell or capture-zone distribution (CZD) and their dependence on the NP size. In general we expect that in the precoalescence regime, the island size or area distribution $N_A(\theta)$ (where $N_A(\theta)$ is the density of islands of area A at coverage θ) may be written in the scaling form [43,44],

$$f(A/\langle A\rangle) = N_A(\theta)\langle A\rangle^2/\theta, \tag{4}$$

where the scaling function $f(x)$ is independent of coverage. In the case of epitaxial growth, an expression for the dependence of the scaled ISD on the critical island size i proposed by Amar and Family (AF) [45],

$$f_i^{\mathrm{AF}}(x) = b_i x^i \exp[-i a_i x^{1/a_i}] \tag{5}$$

(where the constants a_i and b_i satisfy the normalization conditions, $\frac{\Gamma[(i+2)a_i]}{\Gamma[(i+1)a_i]} = (ia_i)^{a_i}$ and $b_i = \frac{(ia_i)^{(i+1)a_i}}{a_i\Gamma[(i+1)a_i]}$) has been widely used to compare with epitaxial growth experiments in which cluster diffusion does not play a significant role. We note that this expression implies that the scaled ISD becomes sharper with increasing critical island size. While more recent work [46–48] (see also Ref. [31]) has shown that the scaled ISD also depends on the island morphology, Eq. (5) has been shown to give reasonable agreement with epitaxial growth experiments as well as simulations for critical island sizes ranging from $i = 1$ to $i = 3$. However, in some cases (such as organic molecule deposition on semiconductor substrates [49,50]) in which coalescence due to cluster diffusion is likely to play an important role, it has been found that the scaled ISDs are better described by a Gamma distribution [see Eq. (7)] with fitting parameter $\beta \simeq 8$–10.

Similarly, the Voronoi cell-size or capture-zone distribution $n_{A_v}(\theta)$ [where $n_{A_v}(\theta)$ is the density of islands with Voronoi-cell area A_v at coverage θ] may be written in the scaling form,

$$C(A_v/\langle A_v\rangle) = \langle A_v\rangle n_{A_v}/N, \tag{6}$$

where N is the island density and $\langle A_v\rangle$ is the average Voronoi area. One form which has been used to fit the scaled CZD in a variety of simulations [51] and experiments [49,50,52–55] is the Gamma distribution,

$$\Gamma_\beta(x) = \frac{\beta^\beta}{\Gamma(\beta)} x^{\beta-1}\exp[-\beta x], \tag{7}$$

where the parameter β satisfies $\beta = \langle x\rangle^2/\sigma^2$ where σ^2 is the variance of the size distribution [49]. More recently Pimpinelli and Einstein [56,57] have proposed an analytical form based on a generalized Wigner distribution (GWD) [58],

$$P_{\beta_W}(x) = a_{\beta_W} x^{\beta_W}\exp(-b_{\beta_W} x^2), \tag{8}$$

where the constants a_{β_W} and b_{β_W} are determined by normalization [59] and $\beta_W = i/\chi$ [60], which implies $\beta_W = i + 2$ [57,61,62] assuming standard nucleation theory.

2. Comparison with experimental results

Figure 6 shows our results for the scaled ISD and CZD for 4.9, 6.0, and 8.0 nm NP sizes, corresponding to the experimental fluxes shown in Fig. 3. As can be seen, in all cases the ISD is sharply peaked despite the existence of significant island diffusion and coalescence. This is in contrast to previous theoretical [16] and simulation [18] results for the case of irreversible island growth ($i = 1$) with cluster diffusion and no barrier to island coalescence for the case $D_A \sim A^{-\mu}$ (where D_A is the mobility of an island of area A) with $\mu \leqslant 1$. On the other hand, recent simulation results [35,36] also indicate that for $i \geqslant 2$ the ISD exhibits a well-defined peak near $A/\langle A\rangle = 1$, even in the presence of significant cluster diffusion and island coalescence. Thus, these results confirm our expectation, based on our analysis in Sec. II B of the scaling of the island density with flux, that in all cases the critical island size is larger than 1.

As shown in Fig. 6(a), there is approximate agreement between the experimental results for the scaled ISD for 8.0 nm NPs and the AF form (5) for $i = 2$. This is consistent with our estimate of the dimer binding energy, which indicates that $i \simeq 2$, as well as with the experimentally estimated value of $\chi \simeq 0.44$, which is close to $1/2$. On the other hand, perhaps due to small-island coalescence [which is not taken into account in Eq. (5)] the experimental scaled ISD is shifted slightly to the left, with a peak at $A/\langle A\rangle < 1$ while the tail of the ISD does not decay as rapidly.

Figure 6(d) shows the corresponding results for the scaled capture zone or Voronoi-cell area distribution. As can be seen, the scaled CZD is somewhat sharper than the scaled ISD. Accordingly, good agreement is found with a Gamma distribution but with a higher value of β ($\beta \simeq 8.0$). We note that this value is similar to that which has been found for the case of organic molecule deposition on semiconductor substrates [49,50]. It is also consistent with suggestions [62–64] that $\beta = 2i + 5$. Also shown in Fig. 6(d) are the generalized Wigner distributions (GWDs) with $\beta_W = i + 2 = 3.6$ and $\beta_W = 4$ (assuming $i = 2$). Both of these distributions give a reasonably good fit to the scaled CZD for 8 nm NPs, although the one for $i = 2$ gives a somewhat better fit. On the other hand, the GWD with either $\beta_W = 1.9$ (corresponding to $i = 0.85$ assuming ALA) or $\beta_W = 8.4$ (corresponding to $i = 3.7$ assuming SCM) do not give good agreement with the experimental CZD and so are not shown. We thus conclude that for 8.0 nm NP islands, both the CZD and the ISD are consistent with $i \simeq 2$ as expected from standard nucleation theory, but are inconsistent with the values of the critical island size expected in the case of ALA or SCM. In addition, we note that the relatively good agreement between the scaled ISD and the scaled CZD suggests that for 8.0 nm NPs both cluster coalescence [18] and island coarsening due to detachment [54] play a relatively minor role.

In contrast, for 6.0 nm and 4.9 nm NPs, the ISDs are broader and less sharply peaked than for 8.0 nm NPs and are also broader than the corresponding CZDs. This result is surprising, since in general one expects that for higher critical island size both the scaled ISD and the scaled CZD will be significantly sharper. As a result, in this case the AF expression Eq. (5) with the corresponding ALA values ($i = 1.6$ and 3.0) or with the even larger SNT values gives poor agreement with the experimental scaled ISDs. Similarly the generalized Wigner distribution with $\beta_W = i + 2$ and the 6.0 nm NP SNT value $i = 4.7$ as well as the corresponding GWD obtained using the 4.9 nm NP ALA value $i = 3.0$ or the even larger SNT values also give poor agreement with the experimental CZDs. One possible explanation for this which is also consistent with the discrepancy between the scaled ISD and the scaled

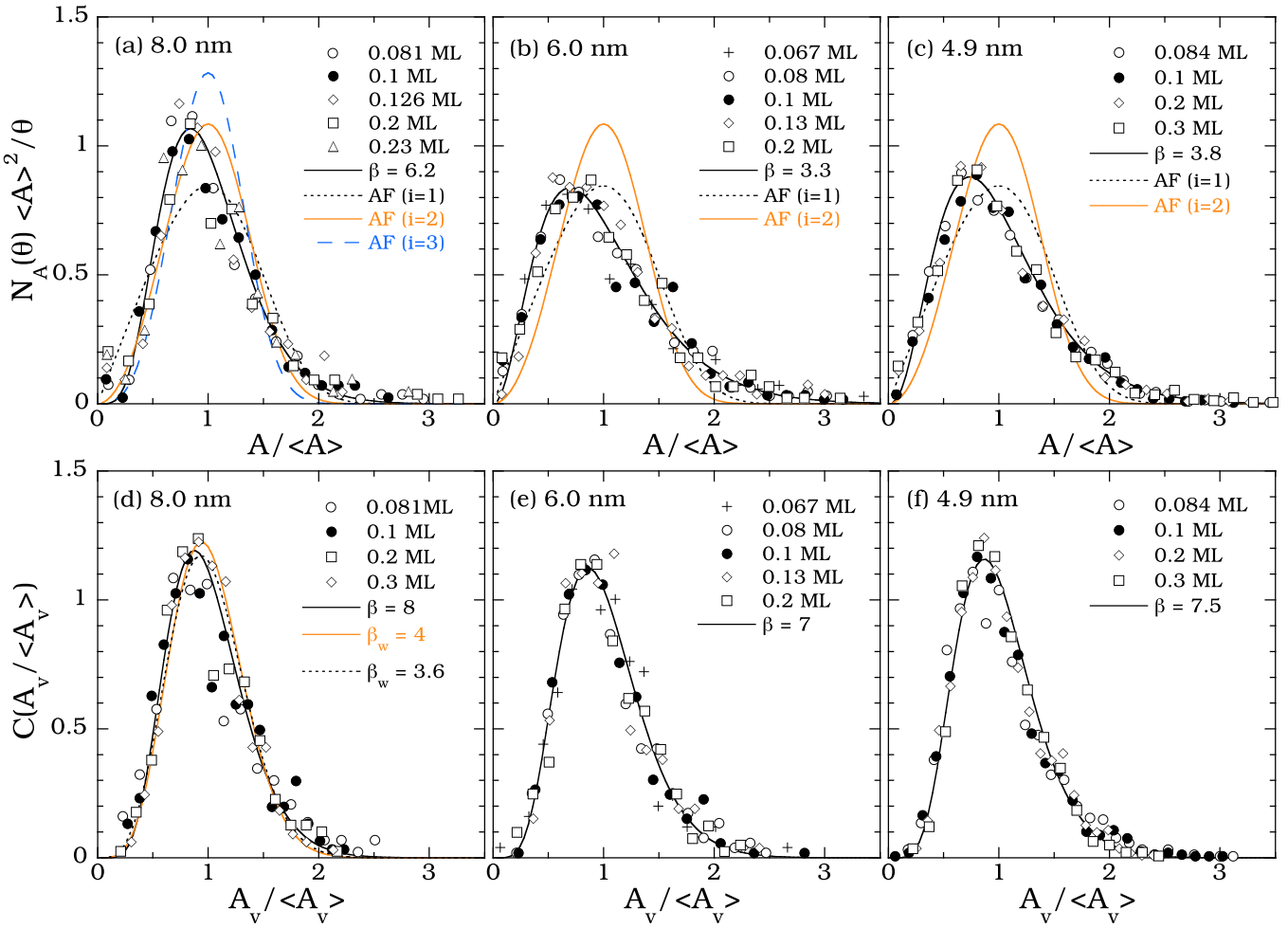

FIG. 6. (Color online) (a)–(c) ISDs and (d)–(f) corresponding CZDs for NP sizes of 8.0 nm, 6.0 nm, and 4.9 nm. Symbols are experimental results, while lines correspond to Eqs. (5), (7), and (8) (see text for details).

CZD, is that, consistent with the results shown in Fig. 3, for 4.9 nm and 6.0 nm NPs, island diffusion and coalescence play a larger role thus reducing the sharpness of the ISD. Another possible explanation is that due to the weaker binding for 4.9 nm and 6.0 nm NPs, there is significant NP detachment even from large islands, and as a result coarsening effects become important [54]. We note that in this case both the ISD and the CZD are reasonably well described by a Gamma distribution $\Gamma_\beta(x)$ but with somewhat smaller values of β than for the case of 8.0 nm NPs. Thus, while our results for the scaled ISD and CZD for 8 nm NPs are roughly consistent with standard epitaxial growth theory, there are significant differences for 4.9 nm and 6.0 nm NPs, which indicate that additional processes such as enhanced cluster coalescence or island coarsening may play an important role. In particular, we expect that cluster coalescence [18] and/or island coarsening due to detachment [54] will broaden the ISD.

D. Island ordering and nearest-neighbor edge-distance distribution

In order to study the effects of LR interactions, we have also investigated the island ordering for 6 nm and 8 nm NPs. Figure 7 shows an optical microscopy image for the case of 6 nm NPs with excess thiol concentration $f = 0.1\%$ and NP concentration $c = 7.8 \times 10^{10}/\mu$l which indicates that at high coverage ($\theta = 0.51$ ML) the islands tend to order, as can be seen by the fact that each island typically has six

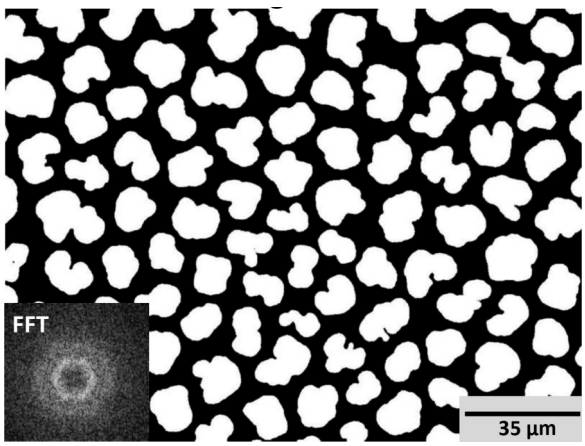

FIG. 7. Optical microscopy image showing island ordering for 6 nm NP islands at $\theta = 0.51$ ml. The inset is a Fourier transform of the image.

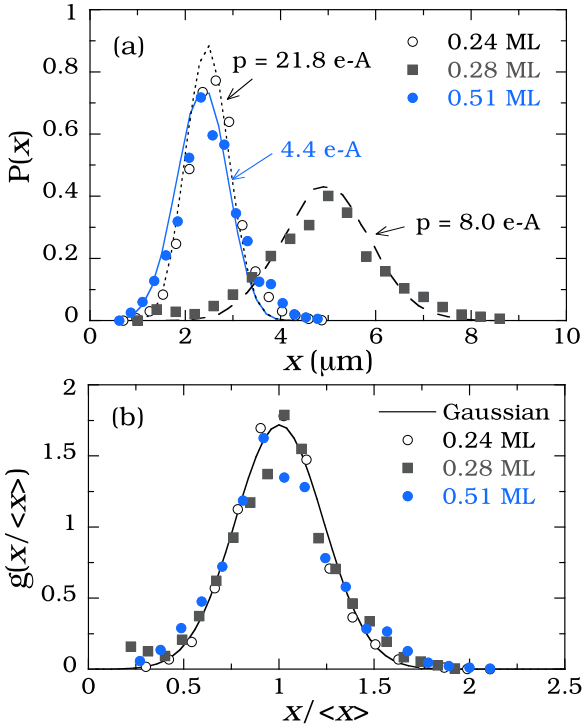

FIG. 8. (Color online) (a) Comparison between experimental results (symbols) for normalized nearest-neighbor edge-distance distribution $P(x)$ with simulation results (solid and dashed curves) based on assumption of a net dipole moment of magnitude p on each NP (see text). Filled symbols correspond to 6 nm NP experiments while open symbols correspond to 8 nm NP experiments. Note that if islands were arranged in an ordered lattice the edge-to-edge distances would be 3.8 μm for 0.24 and 0.51 ML data and 7.6 μm for the 0.28 ML data. (b) Scaled nearest-neighbor edge-distance distribution $g(x/\langle x\rangle)$. The solid line is a Gaussian fit with the values of $\sigma(\theta)$ and $\langle x\rangle$ determined from experimental data for $\theta = 0.24$ ML.

nearest neighbors. The corresponding Fourier transform of the local NP density (see inset) exhibits two well-defined rings, corresponding roughly to the average island distance (inner ring) and average island dimension (outer ring). The sixfold symmetry of the inner ring also indicates the existence of LR orientational ordering.

One possible explanation for this ordering is the existence of island repulsion due to LR interactions, which may also serve to suppress island coalescence. In order to probe the effects of this interaction on the local ordering, we have measured the nearest-neighbor edge-to-edge distance distribution $P(x)$ surrounding each island during growth. Here x is the edge-to-edge distance between a central island and its closest neighbor, while $P(x)$ is the corresponding probability distribution, normalized such that $\int_0^\infty P(x)\,dx = 1$.

As shown in Fig. 8, measurements of $P(x)$ were carried out for 6 nm NPs at $\theta = 0.28$ ML and 0.51 ML under the conditions described above as well as for 8 nm NPs at $\theta = 0.24$ ML with excess thiol concentration $f = 0.01\%$ and NP concentration $c = 3.3 \times 10^{10}/\mu$L. In the latter case the island density ($N = 0.0194\ \mu\text{m}^{-2}$) corresponds to an average island area $\langle A\rangle = 12.5\ \mu\text{m}^2$. In contrast, for the 6 nm NPs, the average island area ranged from $\langle A\rangle = 70.5\ \mu\text{m}^2$ at $\theta = 0.28$ ML to $\langle A\rangle = 104\ \mu\text{m}^2$ at $\theta = 0.51$ ML. As shown in Fig. 8(a), the average *nearest-neighbor* edge distance $\langle x\rangle$ [corresponding to the peaks in $P(x)$] decreases with increasing coverage and is considerably smaller than the expected average edge-to-edge distance (3.8 μm for 0.24 and 0.51 ML data and 7.6 μm for the 0.28 ML data) assuming that the islands are arranged on an ordered triangular lattice. On the other hand, as shown in Fig. 8(b) the scaled distribution $g(x/\langle x\rangle) = \langle x\rangle P(x)$ is approximately Gaussian and independent of coverage and NP size.

E. Long-range repulsion and comparison with Monte Carlo simulations

One possible mechanism for the LR repulsion between islands is the existence of a small dipole moment on each NP which may arise as a result of an asymmetry in the dodecanethiol distribution surrounding the Au core for NPs at the toluene-air interface. In particular, Hartree-Fock calculations for the case of alkanethiols attached to the Au(111) surface [65] indicate that charge transfer between the S and the Au core will lead to a dipole moment of magnitude $\sim$0.44 e· Å for each dodecanethiol attached to the NP. While the thiol distribution is expected to be symmetric for NPs in solution, thus leading to no net dipole moment, for NPs near the interface we expect that, in order to reduce the surface tension, there will be an excess of dodecanethiols attached to the NP near the interface, thus leading to a net dipole moment per NP which is perpendicular to the interface. The resulting dipole moment leads to a LR $1/r^3$ repulsion between NPs which, while too weak to significantly affect the NP island binding, leads to a noticeable repulsion between large NP islands.

In order to determine if our experimental results for the nearest-neighbor edge-distance distribution $P(x)$ may be explained using the assumption of a net dipole moment on each NP, we have carried out off-lattice Monte Carlo simulations of an idealized system in which for simplicity we have assumed that all islands have the same size and are circular with radius $R_1 = \sqrt{\langle A\rangle/\pi}$. The former assumption is a reasonable approximation since the island-size distribution is relatively sharp. Due to the finite-size of the NP core, we expect that an asymmetric thiol distribution may also lead to a small net quadrupole moment. However, for simplicity we have neglected this effect in our simulations.

Using this model we have carried out simulations corresponding to the three different experimental cases shown in Fig. 8 and in each case have adjusted the value of the dipole moment in order to fit the corresponding experimental nearest-neighbor island-distance distribution $P(x)$. Our simulations were carried out using systems with 25–49 islands and periodic boundary conditions, while the system was initialized by placing the islands on a regular triangular lattice with lattice spacing $a_{lat} = (2\langle A\rangle/\sqrt{3}\theta)^{1/2}$ where θ is the measured coverage. The island densities and average island area were the same as in the experiments.

Since, for the relatively large island sizes used in these experiments, the time for island growth is much longer than the typical time for ordering and equilibration as well as the typical observation time used to measure the nearest-neighbor edge-distance distribution, island growth was not

taken into account in our simulations. Accordingly, in our Monte Carlo simulations, we used the Brownian dynamics method described in Ref. [66] in which the displacement $\delta\mathbf{r}$ of each island after a time Δt is given by the Gaussian distribution,

$$P(\delta\mathbf{r},\Delta t)=\frac{1}{4\pi D\Delta t}e^{-|\delta\mathbf{r}-\mathbf{F}_{\rm ext}\Delta t/\gamma|^2/(4D\Delta t)}, \tag{9}$$

where D is the island diffusion coefficient, $1/\gamma = D/(k_{\rm B}T)$, and $\mathbf{F}_{\rm ext}$ corresponds to the net force on each island due to the dipole and van der Waals interaction with all of the other islands. Typical values used in our simulations were $D = 0.01\ \mu{\rm m}^2/{\rm s}$ and $\Delta t = 0.01$ s, while averages were typically taken by first equilibrating for 10^6–10^7 Monte Carlo steps [where one Monte Carlo step corresponds to sequentially going through all of the islands and displacing them using the distribution in Eq. (9)] and then taking data over the same length of time. For comparison, simulations were also carried out with somewhat higher and/or lower values of the island diffusion coefficient and, as expected, the simulated distributions were not affected.

Since the island sizes and distances are much bigger than the NP size, in order to calculate the total force $\mathbf{F}_{\rm ext}$ on each island due to dipole repulsion we have used a continuum approach. Using this approach the dipole interaction energy between two islands may be written as

$$U_{\rm dip}(l)=\frac{p^2}{4\pi\kappa\epsilon_0}n^2I(l), \tag{10}$$

where p is the dipole moment per NP, n is the NP density per unit area in an island [67], and

$$I(l)=\int\int\frac{d^2\mathbf{r}_1d^2\mathbf{r}_2}{|\mathbf{r}_1-\mathbf{r}_2|^3}. \tag{11}$$

Here the integrals are over each island and $I(l)$ depends on the center-to-center distance l and island radius R_1. In addition, if we assume that, consistent with the results of molecular dynamics simulations [22], the Au core remains submerged below the toluene-air interface, then the value of κ may be obtained. In particular, using the expressions in Ref. [68] for the field due to a point charge near an interface to obtain the interaction between two dipoles which are oriented perpendicular to the interface at a distance $|\mathbf{r}_1-\mathbf{r}_2|$ which is much larger than their distance below the interface, we obtain the general expression,

$$\kappa=\frac{\epsilon_2(\epsilon_1+\epsilon_2)}{2\epsilon_1\epsilon_0}, \tag{12}$$

where ϵ_1 (ϵ_2) are the dielectric constants above (below) the interface. Assuming $\epsilon_1\simeq\epsilon_0$ for air and $\epsilon_2\simeq 2.38\,\epsilon_0$ for toluene, we obtain $\kappa\simeq 4.0$. The net force $F(l)$ may then be obtained by differentiating Eq. (10) with respect to l and numerically evaluating either Eq. (11) or its derivative (for details see the Appendix).

Figure 8(a) shows a comparison between the experimental and simulation results. As can be seen, despite the simplifying assumptions of our model, relatively good agreement between the experimentally measured nearest-neighbor edge-distance distributions and simulations may be obtained by assuming a small net dipole moment p on each NP which is oriented normal to the interface. In addition, the values obtained for p are consistent with the expected value of the dipole moment per thiol (approximately 0.44 e· Å) combined with a reasonably small number of "excess" thiols (on the order of 10–20 for the 6 nm NPs and 50 for the 8 nm NPs) on the "top" of the NP (e.g., at the interface) [69,70]. However, the magnitude of the dipole moment appears to decrease with decreasing NP radius as well as with increasing coverage for fixed NP radius. The smaller value of p for 6 nm NPs compared to 8 nm NPs is consistent with the expectation that there will be a smaller number of attached thiols per NP, due to the decreased surface area and number of attachment sites in this case. In contrast, the decrease in the dipole moment with increasing coverage for 6 nm NPs may be explained by the fact that as the toluene evaporates the excess thiol concentration increases and as a result there will be more thiols attached to the bottom of the NP, thus reducing the asymmetry. In addition, the values of p obtained from our simulations are sufficiently small that they have a negligible effect on the island binding energies (which are dominated by the attractive van der Waals and ligand-ligand interactions) and also lead to negligible repulsion for small islands.

While our simulation results are consistent with the existence of a small net dipole moment on each NP which is due to the asymmetry in the attachment of thiols to NPs at the interface, we note that in polar solvents such as water, dipole repulsion may occur even in the presence of a net charge on each NP. For example, in experiments on micron-sized charged polystyrene spheres at the water-oil interface, it has been shown that charge screening combined with the effects of surface tension and electrostatic stress may lead to a SR attraction [71] as well as a longer range effective dipole repulsion [72]. While we do not expect such effects to occur here, in recent experiments [73] on DDT-coated NPs in toluene prepared using a fast synthesis method it was found that the NPs were negatively charged. This method is quite different from that used here, since the Au NPs were first phase transferred from water to hexane (rather than toluene) using acetone (rather than the DDAB surfactant used here) and then transferred to a toluene droplet. Nevertheless, to check for the possibility of a net charge on each NP, we have also carried out simulations in which we assumed that each NP has a net core charge [74]. Our results indicate that for even the smallest possible charge ($|q| = e$), the unscreened Coulomb repulsion is far too strong to account for the experimentally observed nearest-neighbor edge-distance distributions, and also leads to a Coulomb repulsion between nearest-neighbor NPs, which is comparable to the expected binding energy (see Sec. III.B) due to ligand-ligand and van der Waals interactions [15]. Thus, while our simulation results are consistent with the existence of a small net dipole moment on each NP they are not consistent with the existence of a net (unscreened) core charge.

IV. DISCUSSION

In order to gain a better understanding of the effects of nanoparticle interactions and growth conditions on colloidal Au nanoparticle self-assembly, we have studied the dependence of the island density, island-size distribution, and

capture-zone distribution on NP size, excess thiol concentration, coverage, and deposition flux and have compared our results with existing theoretical results for submonolayer epitaxial growth. We have also studied the ordering of NP islands at high coverages and compared with Monte Carlo simulations.

For the case of 8 nm NP islands we found many similarities with epitaxial growth. In particular, we found that the dependence of the island density on flux leads to a value for the flux-density scaling exponent which is roughly consistent with a critical island size equal to 2, corresponding to stable trimers. This result is also consistent with the relatively large estimated dimer binding energy for saturated 8 nm DDT-coated Au NPs in toluene ($E_2/k_BT \simeq 8.5$ at room temperature) obtained using the potential of Khan *et al.* [15], which indicates a relatively small detachment rate for compact islands with three or more NPs.

In addition we have found that for 8 nm NP islands, the island density stays constant up to a relatively high coverage ($\theta \simeq 0.3$ ML) thus indicating that coalescence plays a relatively minor role over this coverage range. Accordingly, the scaled island-size distribution (ISD) is in relatively good agreement with the AF expression [45] for the case of epitaxial growth with critical island size i equal to 2. In this case there is also relatively good agreement between the scaled capture-zone distribution and the scaled ISD. The latter behavior is also consistent with experiments [49] on vapor deposition of pentacene on SiO_2 at high deposition rate for which there was negligible desorption, as well as with experiments on InAs/GaAs growth [54] at temperatures such that there was relatively little detachment from islands. Due to the high binding energy and activation barrier for desorption, both of these conditions are expected to be the case for 8 nm NP islands. We also find reasonable agreement between the generalized Wigner distribution prediction with $\beta_W = i + 2 = 4$ for the scaled CZD and the experimental distribution, in good agreement with epitaxial growth models. On the other hand, a Gamma distribution (with fitting parameter $\beta \simeq 8$) appears to give the best fit with the experimental scaled CZD.

In contrast, for 4.9 nm and 6 nm NP islands, we have found that island coalescence becomes important at somewhat lower coverage, and as a result the island density decreases noticeably over the coverage range $\theta = 0.1$–0.3 ML. In addition, due to the smaller binding energy for 4.9 nm and 6 nm NPs, the effective value of the flux-density scaling exponent ($\chi \simeq 0.7$–1.0) is significantly larger than for 8 nm NPs. These results are consistent with calculations of the dimer binding energy which we have carried out using the potential of Khan *et al.* [15] which indicate that both one-bond and two-bond detachment are significant for 4.9 nm and 6 nm NPs. For 4.9 nm NPs this leads to a significant detachment rate even for islands larger than the "magic" cluster size of 7, thus indicating an effective critical island size larger than 6.

Somewhat surprisingly, we have found that the scaled ISDs for 4.9 nm and 6 nm NP islands are less sharply peaked than for 8 nm NP islands and are also significantly less sharply peaked than expected for such a large critical island size. As a result, while the scaled CZD is similar to that obtained for 8 nm NP islands, there is a significant difference between the scaled ISD and the scaled CZD in this case. One possible explanation for the relatively broad ISD is that, due to the relatively small NP size (which leads to less dipole repulsion between islands) there is significantly more island coalescence. The increased island coalescence in the nucleation regime tends to smear out the peak near $A/\langle A \rangle = 1$ in the island-size distribution, in a manner similar to that which was previously found in simulations of irreversible island growth ($i = 1$) with cluster diffusion [18,19]. In addition, due to the weaker binding in this case, there is significant NP detachment from large islands, and as a result we expect that coarsening effects [75] may also play a role [54].

In addition to the scaling of the island density, island size and capture-zone distributions, we have also studied the effects of LR interactions on island ordering. In particular, both the LR orientational ordering observed for 6 nm NP islands at high coverage as well as our results for the nearest-neighbor edge-distance distributions for 6 nm and 8 nm NP islands, indicate the existence of a repulsive interaction between islands. One possible mechanism for this repulsion is the existence of a small dipole moment on each NP which arises as a result of an asymmetry, driven by surface tension, in the thiol distribution for NPs adsorbed at the toluene-air interface. While such a dipole interaction leads to a repulsion between NPs which is negligible at short distances compared to the van der Waals and ligand-ligand interaction, due to the fact that it decays more slowly than the van der Waals interaction, for large islands it can lead to significant island repulsion at large distances.

The existence of such a dipole interaction is supported by the fact that the value needed to obtain good agreement with the experimental nearest-neighbor edge-distance distance distributions corresponds to a relatively small asymmetry (on the order of 10–20 for the 6 nm NPs and 50 for the 8 nm NPs) between the number of thiols on the "top" of the NP and on the bottom of the NP. The larger dipole moment obtained for 8 nm NPs compared to 6 nm NPs is also consistent with this picture, while the decrease in the dipole moment with increasing coverage is consistent with the expected reduction in thiol asymmetry as the excess thiol concentration increases due to droplet evaporation. The decrease of the strength of the repulsive interaction with decreasing NP size is also consistent with our experimental observations that there is significantly more island coalescence for 4.9 nm and 6.0 nm NP islands than for 8.0 nm NP islands.

Finally, we note that while our analysis of the self-assembly process has focused primarily on NP interactions, some additional factors may also play a role. In particular, as already noted in Sec. II, during the drop-drying process there are interfacial flows near the edge of the droplet. While we expect that in the early stages of island nucleation and growth the diffusion of small clusters will be dominated by Brownian diffusion, these flows or inhomogeneities may significantly enhance diffusion for larger clusters and thus contribute to the nonthermal coalescence of large islands. Accordingly, the estimate of the NP dipole moment obtained from our Monte Carlo simulations may actually be a lower bound.

In conclusion, we find that both SR and LR interactions play an important role in NP island self-assembly, while the strength of these interactions increases with NP size. In particular, the SR attractive ligand-ligand and van der

Waals interactions determine the critical island size, while LR repulsive interactions affect the later stage island ordering and coalescence. As a result, the scaling of the island density, ISD, and CZD, as well as the NP island ordering, all depend significantly on NP size. In the future, it would be of interest to carry out more detailed simulations of island nucleation and growth which take these interactions into account, in order to understand in more detail the process of NP self-assembly.

ACKNOWLEDGMENTS

We would like to acknowledge useful discussions with Robert T. Deck. This work was supported by the National Science Foundation under Grant No. CHE-1012896.

APPENDIX

While Eq. (11) may be directly evaluated numerically as a function of center-to-center separation l, it is convenient to first reduce it to two one-dimensional integrals using methods similar to those used in Ref. [12]. In particular, the $1/r^3$ interaction between a point P on circular island 2 (which is a distance R away from the center of circular island 1; see Fig. 9), and all of the points of island 1 which are a distance r away may be written as $\frac{2r\theta(R,r)}{r^3}$ where $\theta(x,y)$ is defined as the half-angle at a point which is a distance x from the center of a disk of radius R_1, corresponding to an arc of radius y passing through the disk. Integrating over all possible values of r for each R, and then integrating over all possible values of R, we may write

$$I(l) = \int_{l-R_1}^{l+R_1} dR[2R\,\theta(l,R)] \int_{R-R_1}^{R+R_1} dr \frac{2r\theta(R,r)}{r^3}, \quad \text{(A1)}$$

where $\theta(x,y)$ is defined as the half-angle at a point which is a distance x from the center of a disk of radius R_1, corresponding to an arc of radius y passing through the disk. Using the cosine law one may write

$$\theta(x,y) = \cos^{-1}\left(\frac{x^2+y^2-R_1^2}{2xy}\right), \quad \text{(A2)}$$

which implies $\theta(l,R) = \cos^{-1}(\frac{l^2+R^2-R_1^2}{2lR})$ and $\theta(R,r) = \cos^{-1}(\frac{R^2+r^2-R_1^2}{2Rr})$. Converting to dimensionless variables $u = R/R_1, v = r/R_1, \alpha = l/R_1$ with $\beta^2 \equiv 1-u^2$, we obtain

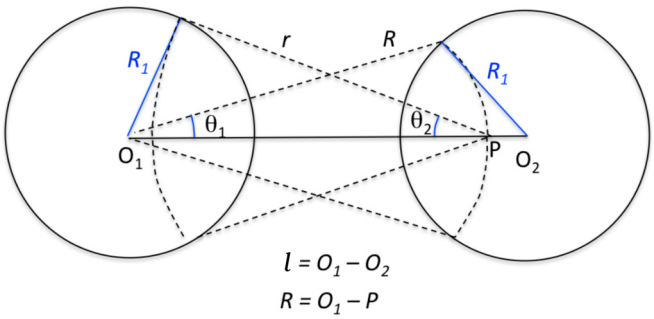

FIG. 9. (Color online) Schematic showing geometry used in converting four-dimensional integral in Eq. (11) to a two-dimensional integral as in Eq. (A1).

$$I(l) = 4R_1 \int_{\alpha-1}^{\alpha+1} du\,u \cos^{-1}\left(\frac{\alpha^2-\beta^2}{2u\alpha}\right) \times \int_{u-1}^{u+1} \frac{dv \cos^{-1}\left(\frac{v^2-\beta^2}{2uv}\right)}{v^2}. \quad \text{(A3)}$$

The net radial repulsive force on a disk of radius R_1 due to another disk of radius R_1 which is a distance l away is then given by

$$F(l) = -\frac{p^2}{4\pi\kappa\epsilon_0}\frac{n^2}{R_1}\frac{\partial I(l)}{\partial\alpha}, \quad \text{(A4)}$$

which may be rewritten as

$$F(l) = \frac{p^2n^2}{\pi\kappa\epsilon_0} J(\alpha), \quad \text{(A5)}$$

where

$$J(\alpha) = \int_{\alpha-1}^{\alpha+1} \frac{du(\beta^2+\alpha^2)}{2\alpha^2\sqrt{1-\left(\frac{\beta^2-\alpha^2}{2u\alpha}\right)^2}} \int_{u-1}^{u+1} \frac{dv \cos^{-1}\left(\frac{v^2-\beta^2}{2uv}\right)}{v^2}. \quad \text{(A6)}$$

A similar approach may be used to calculate the van der Waals force between two circular NP islands of radius R_1 as a function of their center-to-center distance l. However, for the separations of relevance in our simulations this contribution is negligible since the van der Waals attraction decays much more rapidly at large distances than the dipole repulsion.

[1] X.-M. Lin, H. M. Jaeger, C. M. Sorensen, and K. J. Klabunde, J. Phys. Chem. B **105**, 3353 (2001).
[2] S. Narayanan, J. Wang, and X.-M. Lin, Phys. Rev. Lett. **93**, 135503 (2004).
[3] T. P. Bigioni, X.-M. Lin, T. T. Nguyen, E. I. Corwin, T. A. Witten, and H. M. Jaeger, Nat. Mater. **5**, 265 (2006).
[4] A. Snezhko, J. Phys.: Condens. Matter **23**, 153101 (2011).
[5] H. Alhummiany, S. Jarvis, R. A. J. Woolley, A. Stannard, M. Blunt, and P. Moriarty, J. Mater. Chem. **21**, 16983 (2011).
[6] A. Stannard, J. Phys.: Condens. Matter **23**, 083001 (2011).
[7] D. Vanmaekelbergh, Nano Today **6**, 419 (2011).
[8] M. J. Robbins, A. J. Archer, and U. Thiele, J. Phys.: Condens. Matter **23**, 415102 (2011).
[9] J. Park, H. Zheng, W. C. Lee, P. L. Geissler, E. Rabani, and A. P. Alivisatos, ACS Nano **6**, 2078 (2012).
[10] S.-K. Eah, J. Mater. Chem. **21**, 16866 (2011).
[11] J. Wu, H. Zhang, J. Zhang, T. Yao, H. Sun, and B. Yang, Colloids Surface A **348**, 240 (2009).
[12] H. C. Hamaker, Physica (Utrecht) **4**, 1058 (1937).
[13] R. J. Hunter, *Foundation of Colloid Science* (Oxford University Press, New York, 2001).
[14] I. D. Morrison and S. Ross, *Colloidal Dispersions: Suspensions, Emulsion, and Foams* (Wiley, New York, 2002).
[15] S. J. Khan, F. Pierce, C. M. Sorensen, and A. Chakrabarti, Langmuir **25**, 13861 (2009).

[16] P. L. Krapivsky, J. F. F. Mendes, and S. Redner, Eur. Phys. J. B **4**, 401 (1998).

[17] P. L. Krapivsky, J. F. F. Mendes, and S. Redner, Phys. Rev. B **59**, 15950 (1999).

[18] Y. A. Kryukov and J. G. Amar, Phys. Rev. E **83**, 041611 (2011).

[19] B. C. Hubartt, Y. A. Kryukov, and J. G. Amar, Phys. Rev. E **84**, 021604 (2011).

[20] X. M. Lin, C. M. Sorensen, and K. J. Klabunde, J. Nanopart. Res. **2**, 157 (2000).

[21] X. M. Lin, C. M. Sorensen, and K. J. Klabunde, Chem. Mater. **11**, 198 (1999).

[22] N. N. Poddar and J. G. Amar, J. Chem. Phys. **140**, 244702 (2014).

[23] X. Yu, P. M. Duxbury, G. Jeffers, and M. A. Dubson, Phys. Rev. B **44**, 13163 (1991).

[24] J. A. Venables, G. D. Spiller, and M. Hanbücken, Rep. Prog. Phys. **47**, 399 (1984).

[25] J. A. Stroscio and D. T. Pierce, Phys. Rev. B **49**, 8522 (1994).

[26] A. R. Avery, H. T. Dobbs, D. M. Holmes, B. A. Joyce, and D. D. Vvedensky, Phys. Rev. Lett. **79**, 3938 (1997).

[27] Y. Ebiko, S. Muto, D. Suzuki, S. Itoh, K. Shiramine, T. Haga, Y. Nakata, and N. Yokoyama, Phys. Rev. Lett. **80**, 2650 (1998).

[28] H. Brune, G. S. Bales, J. Jacobsen, C. Boragno, and K. Kern, Phys. Rev. B **60**, 5991 (1999).

[29] H. Zheng, M. H. Xie, H. S. Wu, and Q. K. Xue, Phys. Rev. B **77**, 045303 (2008).

[30] F. Arciprete, E. Placidi, V. Sessi, M. Fanfoni, F. Patella, and A. Balzarotti, Appl. Phys. Lett. **89**, 041904 (2006).

[31] J. W. Evans, P. A. Thiel, and M. C. Bartelt, Surf. Sci. Rep. **61**, 1 (2006).

[32] NP concentrations ranged from $5.5 \times 10^{10}/\mu$l to $3.2 \times 10^{11}/\mu$l for 4.9 nm NPs, $1.7 \times 10^{10}/\mu$l to $1.8 \times 10^{11}/\mu$l for 6.0 nm NPs, and $2.5 \times 10^{10}/\mu$l to $7.0 \times 10^{10}/\mu$l for 8.0 nm NPs.

[33] M. Schroeder and D. E. Wolf, Phys. Rev. Lett. **74**, 2062 (1995).

[34] P. A. Mulheran and D. A. Robbie, Phys. Rev. B **64**, 115402 (2001).

[35] Y. A. Kryukov, Ph.D. thesis, University of Toledo (2011). See also https://etd.ohiolink.edu/ap/1?0.

[36] B. C. Hubartt, J. Jin, and J. G. Amar (unpublished).

[37] D. Kandel, Phys. Rev. Lett. **78**, 499 (1997).

[38] J. A. Venables and H. Brune, Phys. Rev. B **66**, 195404 (2002).

[39] J. Villain, A. Pimpinelli, L. Tang, and D. Wolf, J. Phys. (France) I **2**, 2107 (1992).

[40] I. Furman and O. Biham, Phys. Rev. B **55**, 7917 (1997).

[41] P. Jensen, H. Larralde, and A. Pimpinelli, Phys. Rev. B **55**, 2556 (1997).

[42] D. Walton, J. Chem. Phys. **37**, 2182 (1962); D. Walton, T. Rhodin, and R. W. Rollins, *ibid.* **38**, 2698 (1963).

[43] M. C. Bartelt and J. W. Evans, Surf. Sci. **298**, 421 (1993).

[44] J. G. Amar, F. Family, and P.-M. Lam, Phys. Rev. B **50**, 8781 (1994).

[45] J. G. Amar and F. Family, Phys. Rev. Lett. **74**, 2066 (1995).

[46] J. G. Amar and F. Family, Mater. Res. Soc. Symp. Proc. **367**, 149 (1995).

[47] M. N. Popescu, J. G. Amar, and F. Family, Phys. Rev. B **64**, 205404 (2001).

[48] T. J. Oliveira and F. D. A. Aarão Reis, Phys. Rev. B **83**, 201405 (2011).

[49] S. Pratontep, M. Brinkmann, F. Nüesch, and L. Zuppiroli, Phys. Rev. B **69**, 165201 (2004).

[50] M. Brinkmann, F. Biscarini, C. Taliani, I. Aiello, and M. Ghedini, Phys. Rev. B **61**, R16339 (2000).

[51] P. A. Mulheran and J. A. Blackman, Phys. Rev. B **53**, 10261 (1996).

[52] M. Fanfoni, E. Placidi, F. Arciprete, E. Orsini, F. Patella, and A. Balzarotti, Phys. Rev. B **75**, 245312 (2007).

[53] S. Miyamoto, O. Moutanabbir, E. E. Haller, and K. M. Itoh, Phys. Rev. B **79**, 165415 (2009).

[54] M. Fanfoni, F. Arciprete, C. Tirabassi, D. Del Gaudio, A. Filabozzi, A. Balzarotti, F. Patella, and E. Placidi, Phys. Rev. E **86**, 061605 (2012).

[55] R. A. Puglisi, G. Nicotra, S. Lombardo, C. Spinella, G. Ammendola, and C. Gerardi, Phys. Rev. B **71**, 125322 (2005).

[56] A. Pimpinelli and T. L. Einstein, Phys. Rev. Lett. **99**, 226102 (2007).

[57] A. Pimpinelli and T. L. Einstein, Phys. Rev. Lett. **104**, 149602 (2010).

[58] T. Guhr, A. Müller-Groeling, and H. A. Weidenmüller, Phys. Rep. **299**, 189 (1998).

[59] $a_{\beta_W} = 2\Gamma(\frac{\beta_W+2}{2})^{\beta_W+1}/\,\Gamma(\frac{\beta_W+1}{2})^{\beta_W+2}$ and $b_{\beta_W} = [\Gamma(\frac{\beta_W+2}{2})/\Gamma(\frac{\beta_W+1}{2})]^2$.

[60] A. Pimpinelli, L. Tumbek, and A. Winkler, J. Phys. Chem. Lett. **5**, 995 (2014).

[61] F. Shi, Y. Shim, and J. G. Amar, Phys. Rev. E **79**, 011602 (2009).

[62] M. Li, Y. Han, and J. W. Evans, Phys. Rev. Lett. **104**, 149601 (2010).

[63] R. Sathiyanarayanan, A. BH. Hamouda, A. Pimpinelli, T. L. Einstein, Phys. Rev. B **83**, 035424 (2011).

[64] M. A. Groce, B. R. Conrad, W. G. Cullen, A. Pimpinelli, E. D. Williams, and T. L. Einstein, Surf. Sci. **606**, 53 (2012).

[65] D. M. Alloway, M. Hofmann, D. L. Smith, N. E. Gruhn, A. L. Graham, R. Colorado, Jr., V. H. Wysocki, T. R. Lee, P. A. Lee, and N. R. Armstrong, J. Phys. Chem. B **107**, 11690 (2003).

[66] J. C. Fernández-Toledano, A. Moncho-Jordá, F. Martinez-López, A. E. González, and R. Hidalgo-Álvarez, Phys. Rev. E **75**, 041408 (2007).

[67] In agreement with experiment we assume that the NPs in each island are arranged on a triangular lattice with a lattice constant of 8.0 nm (9.6 nm) for 6 nm (8 nm) NPs.

[68] M. A. Mohammed, E. F. Kuester, M. Piket-May, and C. L. Holloway, Prog. Electromag. Res. B **16**, 1 (2009).

[69] The total number of thiols attached to each NP may be estimated based on a saturation thiol density of $4.77/\text{nm}^2$ [70], to be approximately 540 (960) dodecanethiols for 6 nm (8 nm) NPs.

[70] G. H. Woehrle, L. O. Brown, and J. E. Hutchison, J. Am Chem. Soc. **127**, 2172 (2005).

[71] M. G. Nikolaides, A. R. Bausch, M. F. Hsu, A. D. Dinsmore, M. P. Brenner, C. Gay, and D. A. Weitz, Nature (London) **420**, 299 (2002).

[72] P. Pieranski, Phys. Rev. Lett. **45**, 569 (1980).

[73] M. N. Martin, J. I. Basham, P. Chando, and S.-K. Eah, Langmuir **26**, 7410 (2010).

[74] In this case the Coulomb interaction between two charged NPs which are separated by a distance r which is much larger than their distance below the interface is given by $U(r) = \frac{e^2}{4\pi\epsilon' r}$ where $\epsilon' = (\epsilon_{\text{air}} + \epsilon_{\text{tol}})/2 \simeq 1.69\epsilon_0$ [68].

[75] F. Shi, Y. Shim, and J. G. Amar, Phys. Rev. E **76**, 031607 (2007).